An in-situ FTIR spectroscopic and thermogravimetric analysis study of the dehydration and dihydroxylation of SnO_2: the contribution of the (100), (110) and (111) facets

P. A. Christensen*[1], P. S. Attidekou[1], R. G. Egdell[2], S. Maneelok[1] and D. A. C. Manning[3].
1 School of Chemical and Process Engineering, Bedson Building, Newcastle University, Newcastle upon Tyne, NE1 7RU, UK.
2. Department of Chemistry, University of Oxford, Inorganic Chemistry Laboratory, South Parks Road, Oxford OX1 3QR, UK.
3. School of Civil Engineering and Geosciences, Drummond Building, Newcastle University, Newcastle upon Tyne, NE1 7RU, UK.

ABSTRACT
Nanoparticulate SnO_2 produced by a hydrothermal method was characterised by BET, XRD, TGA-MS and in-situ variable temperature Diffuse Reflectance Infra Red Spectroscopy (DRIFTS) to determine the surface behaviour of water. For the (100) facets, hydrogen bonding does not occur, and water absorption is less strong than for the (111) and (110) facets where hydrogen bonding does occur. Reversible uptake of oxygen was observed. These findings have implications for other surface-gas reactions in which Ni and Sb co-doped SnO_2 (NATO) anodes are used for ozone generation. BET showed the relatively high surface area and nanometer scale of the SnO_2 particles, whilst XRD confirmed the nano dimension of the crystallites and showed only the cassiterite phase. TGA analysis indicated four temperature regions over which mass loss was observed. These and the in-situ DRIFTS studies revealed the existence of various forms of water associated with specific crystal facets of the SnO_2, as well as the existence of isolated O-H groups and adsorbed oxygen species. Electronic absorptions were also observed and the data rationalised in terms of the existence of both free electron absorptions, and absorptions from oxygen vacancy states. The role of adsorbed molecular oxygen in electrochemical ozone generation at Ni and Sb co-doped SnO_2 (NATO) anodes was strongly suggested by this work.

1. INTRODUCTION
Ozone is regarded as a "chemical-free" cleaning and sterilization agent as it reacts to produce only oxygen. It thus has potential application in a wide range of industrial, domestic and health environments that include water treatment, white goods, hospitals and fertility clinics. As an example, with respect to the latter, there is increasing evidence that conventional chemical cleaning agents can give rise to Volatile Organic Compounds (VOCs) and that these can be harmful to embryos and have a detrimental effect upon pregnancy rates[1].

The standard methods of ozone generation, dielectric barrier discharge or cold corona discharge, are not portable as they require high voltages and, preferably, pure oxygen feeds to avoid NOx formation[2]. They also produce ozone only in the gas phase, which then must be dissolved in water. In contrast, the electrochemical generation of ozone has many advantages including: low voltage operation, the potential to generate ozone in the gas and liquid phases, no need for gas feeds of any description and robust, simple and portable system design. The drawbacks have been: low current efficiencies of common catalysts such as PbO_2, and the high operating voltages and uncertainty surrounding Boron Doped Diamond (BDD) anodes. BDD anodes are the only other anodes (apart from NATO, see below) which have been reported as having very high ozone activity, although ozone activity appears to be the exception rather than the rule, such anodes generally being employed for direct oxidation[2].

In 2004 Chan and co-workers[3, 4] reported that adding trace amounts of Ni to Sb-doped SnO_2 anodes supported on Ti mesh transformed the previously inactive Sb-SnO_2 into an anode exhibiting a

current efficiency of 0.35 towards the generation of ozone (O_3) at room temperature in aqueous sulfuric acid with a cell voltage below 3V. Optimal activity was found with a Sn:Sb:Ni molar ratio of 500:8:1. The realisation of very high O_3 activity simply through the addition of small amounts of Ni was unexpected. Subsequently, nickel and antinomy-doped SnO_2 (NATO) anodes have shown current efficiencies up to 0.5[5] and current densities of 100 mA cm^{-2} and lifetimes in excess of 250 hours[2]. The lifetime observed is remarkable, given that Ni is unstable with respect to Ni^{2+} in acidic solutions, particularly at anodic potentials[6]. The challenges with respect to these materials are irreproducible synthesis and low current densities. With respect to the latter, without high proton fluxes (ie high current densities: zero gap cells employing PbO_2 anodes typically achieve current densities around 1 A cm^{-2})[2], and the resistance of polymer electrolyte membranes increases due to the much lower mobility of the cations found in water (e.g. Na^+, Ca^{2+}) compared to protons, demanding the use of de-ionised water, which is not a viable option. If active and selective nanoparticulate NATO anodes can be fabricated, this should allow operation at high geometric current densities and hence overcome the problem of cations in "real" waters. Further, the methodology employed to synthesize the particulate catalysts should prove easier to control and employ in a reproducible fashion compared to that generally used to produce the ceramic anodes, which consists of dip-coating Ti substrates into catalyst precursor solution followed by calcining[2].

The mechanism by which O_3 evolution takes place at Ni/Sb-SnO_2 anodes remains obscure, not least because the level and mode of Ni incorporation into the anode has yet to be established. It has been postulated that the active site involves Ni(III), but this hypothesis is not supported by any experimental evidence[7, 8], and other workers have found evidence only for Ni(II)[9].

Until definitive and quantitative analytical evidence is available on the composition of Ni/Sb-SnO_2 anodes and structure/activity correlations have been made, attempts to understand the mechanism of ozone generation at these materials will remain speculative. ~~This paper is the first of two focussed on identifying the active site of NATO anodes and hence the mechanism of ozone generation. The strategy was to synthesize SnO_2, Sb-SnO_2 and NATO nanopowders~~ In order to identify the active site for ozone generation at NATO anodes, it was decided to adopt a step-by-step approach by carrying out full characterization using surface area determination by gas adsorption, powder X-ray diffraction (XRD), Fourier Transform InfraRed (FTIR) spectroscopy and thermogravimetric analysis coupled with evolved gas analysis by mass spectrometry (TGA) to investigate the structural and other changes induced by doping SnO_2 first with Sb then with varying amounts of nickel, and to correlate the latter with ozone activity and selectivity. This paper reports the initial benchmarking studies on SnO_2. It provides fundamental information concerning the reactions that take place at specific crystal facets that control water adsorption, and so reports essential information required to interpret the mechanisms of other surface catalytic phenomena on SnO_2, including ozone generation.

2. METHODS

SnO_2 nanopowders were prepared by hydrothermal synthesis using a method adapted from that of Fujihara and co-workers[10]. A 0.1M solution of $SnCl_4.5H_2O$ (98%, Sigma-Aldrich), was prepared in 200 cm^3 deionised water (Millipore Milli-Q, 18 MΩ cm) and refluxed at 95 °C for 3 hours to promote hydrolysis and formation of SnO_2. Following refluxing, the nanoparticulate SnO_2 precipitate was recovered by centrifuging and washed 25 times with water until chloride had been removed completely (as determined by the absence of a precipitate upon addition of aqueous 0.1M $AgNO_3$). The powder was then placed in a Teflon vessel in an autoclave and heated at180 °C (generating a pressure of 10 bar) for 24 hours, after which it was washed with water until no further chloride appeared (as above). After drying, the powder was calcined 400 °C for 1 hour at a step rate of 5 °C min^{-1} before cooling down to room temperature.

Powder diffraction patterns were measured on a PANalytical X'Pert Pro MPD diffractometer, powered by a Philips PW3040/60 X-ray generator operated at 40 kV with 40 mA emission current, generating monochromatic Cu Kα radiation, and incorporating an X'Celerator detector. Diffraction peaks were acquired between 2θ = 10 to 60° and were assigned using the ICSD crystallographic data base. The peaks at 2θ = 26.43°, 33.58° and 51.49° were employed to determine crystallite size.

TGA analyses were carried out in an atmosphere of flowing (40 cm^3 min^{-1}) air, in a Netzsch STA 449C TG-DSC (thermogravimetry-differential scanning calorimetry, or TG-DSC) system, connected to a Netzsch Aeolos 403C quadrupole mass spectrometer (QMS; m/z range 10-300). Samples were loaded into alumina crucibles (approximately 30-40 mg sample mass). A heating rate of 5 °C min^{-1} was used from 25 °C – 900 °C, held at 900 °C for 10 minutes then cooled at 5 °C min^{-1} to room temperature.

The surface area of the SnO_2 powder was determined with a Thermo Scientific Surfer analyser using multipoint Brunauer Emmett and Teller (BET) adsorption isotherms. The sample of mass 75 mg was prepared by degassing at 250 °C for 3 hours with a ramp rate of 5 °C min^{-1} to reach this temperature prior to N_2 adsorption.

In-situ FTIR experiments were carried out using a Varian 670-IR spectrometer equipped with a ceramic air-cooled infrared source, a cooled DLaTGS detector and a Specac Environmental Chamber and diffuse reflectance unit[11]. 20 mg of SnO_2 were mixed with 80 mg of spectroscopic grade KBr (Sigma-Aldrich). The Specac reflectance accessory allows IR spectra to be collected under controlled atmosphere conditions from room temperature to 600 °C and pressures from vacuum to 34 atm. The IR beam is incident on the sample in the cell at angles from 20° to 76° with respect to the horizontal plane via a ZnSe window.

Spectra were recorded in reflectance mode and then converted to an effective absorption using the Kubelka-Munk equation. Thus a reference spectrum (S_R, 100 co-added scans and averaged scans at 8 cm^{-1} resolution, ca. 2 minutes per scanset) was collected from pure KBr at room temperature. The KBr was then replaced with the SnO_2/KBr sample and a spectrum collected at 25 °C. The temperature of the sample was then increased at 5 °C min^{-1} and a further spectrum collected at 50 ºC, after which spectra S_T were collected every 50 ºC up to 600 ºC. The spectra were manipulated as:

$$R_T = (S_R/S_T) \quad (1)$$

$$\text{Kubelka-Munk function } KM = (1-R_T)^2/2R_T \quad (2)$$

and the Kubelka-Munk function[12] plotted vs wavenumber.

This data manipulation results in difference spectra in which peaks with positive amplitude arise from the gain of absorbing species in S_S with respect to S_R, and peaks with negative amplitude to the loss of absorbing species. Difference spectra were simply subtracted from each other (eg $KM_{600C} - KM_{300C}$); ie. no subtraction factor was employed.

3. RESULTS AND DISCUSSION

3.1 Surface Area and Structural Characterisation

BET measurements gave a surface area of 50 m^2 g^{-1} for the SnO_2 powder, and the XRD data showed the structure to be that of tetragonal cassiterite which has the rutile structure (Cassiterite,

syn; Q: S; 00-041-1445), see Fig. S1. As can be seen, peaks due to the (110), (101), (020), (121) and (220) reflections were observed; (200) or (020) are the allowed second order reflections from (100) or (010) oriented crystallites. The XRD line broadening corresponded to a crystallite size of 14.5 nm according to the Scherrer equation. Crystallite size appears to correspond to particle size, giving a surface area (based on a density of 6.95 g cm^{-3} and assuming spherical crystallites[13], (see SEM image in Fig. S2) of 60 m^2 g^{-1}, comparable to that obtained from the BET.

3.2 TGA Studies

Fig. 1(a) shows the TGA response from 45.7 mg of SnO_2, and Fig. 1(b) the differential of the plot. Fig. 2 shows the m/z = 18 response, the only mass spectrometer response observed during the heating process, suggesting that water is the only species evolved during the heating of the SnO_2 sample. As can be seen, the maxima in the m/z = 18 ion current occur at the same temperatures as the minima in the differential plots. From the figures it is possible to distinguish regions with limits at 25 °C - 63 °C, 63 °C - 150 °C, 150 °C – 450 °C and 450 °C – 900 °C delineated by the minima in the differential mass loss. The mass loss up to 150 °C is due to the loss of adsorbed molecular water[14, 15], which is complete by 150 °C. The mass loss at higher temperatures is also highly likely to be due to the loss of water, given the absence of any other species in the mass spectra: the most probable process taking place is the dehydration of SnOH groups[14-16]:

$$2SnOH \rightarrow Sn\text{-}O\text{-}Sn + H_2O \quad (3)$$

On the basis of the mass loss up to 150 °C, and employing an area of ca. 15 x 10^{-20} m^2 for the water molecule[14] (derived from BET studies on TiO_2 rutile which has the same structure as SnO_2[17]) the coverage of the SnO_2 particles by water at 25 °C is ca. 0.39 of a monolayer, suggesting that the form of the water is not that of the bulk liquid. This is in agreement with the work of Morishige *et al.*[18] and Morimoto *et al.*,[19, 20] who have suggested that fully hydroxylated SnO_2 surfaces can be thought of as essentially hydrophobic as they adsorb water only sparsely, i. e. one water molecule to 3 or 4 OH groups. There is an inflexion in the Fig. 1(a) around 300 ºC, which appears as a shoulder on the 450 ºC peak in Fig. 1(b). Higgins and co-workers attributed such an inflexion in the TGA of yttrium-doped barium zirconate to the uptake of oxygen[21].

Wang and co-workers[22] employed TGA to study fully hydrated SnO_2 nanoparticles produced by precipitation at 100 °C. Their TGA and differential TGA curves were qualitatively similar to those shown in Figs. 1(a) and (b), except that the mass loss up to 150 °C was 7% compared to 0.4% found here. It was decided to study the processes taking place in the absence of significant hydration, and this led to the experiment depicted in Figs. 3(a) and (b) where a SnO_2 sample was subjected to four successive heating and cooling cycles to remove the adsorbed water and reveal any underlying processes. Fig. 3(a) shows runs 1, 2 and 4 (run 3 omitted for clarity); run 1 closely resembles the TGA response in Fig. 1(a), as expected. However, runs 2 and 4 show markedly different behaviour, as may be seen from Fig. 3(b) which shows only the response obtained during run 4. Fig. 3(b) shows an initial increase in mass with a pronounced maximum (region (I)), followed by a sharp decrease to c.a. 450 ºC (region (II)) and then a slower decrease in mass to 900 ºC, region (III). On cooling, region (IV) there is a steady increase in mass. The % mass loss in each region is ca. 0.1%.

In all the runs in Fig. 3(a), the mass gain on cooling was 0.12 ± 0.02% and the mass returned to its original value (100% = 56 mg) suggesting that, once water is removed, the process(es) responsible for the temperature-dependent mass change is/are reversible. As was observed in Fig. 1(a), there is an inflexion in the response observed during heating in run 1 around 300 ºC; this corresponds to the maximum in Fig 3(b). Thus, it does not seem unreasonable to attribute the behaviour in Fig 3(b) to the reversible uptake of oxygen[21]: it is generally accepted that oxygen adsorbs on the surface of SnO_2, and can then diffuse into the inner grain boundary surfaces of porous SnO_2[23, 24] where it

adsorbs and modifies the potential barriers between the grains. There is considerable hysteresis in the TGA responses during runs 2 and 4, and it appears that the O_2 uptake in region (I) is lost again in region (II). This is followed by further O_2 loss in region (III), which probably extends back into region (II), with a lower temperature coefficient. The O_2 lost in region (III) is then restored in region (IV), with approximately the same temperature coefficient as region (III). The mass of the sample returns to its starting value on cooling, suggesting the changes are reversible. A 0.1% change in mass corresponds to a coverage of Sn by oxygen atoms of 0.04, using the BET surface area of 50 m^2 g^{-1} and assuming 9.1 x 10^{14} Sn atoms cm^{-2} [24].

The adsorption of molecular oxygen has direct relevance to the electrochemical production of ozone at Ni/Sb-SnO_2 anodes, with most ozone mechanisms involving the reaction of oxygen atoms with adsorbed molecular oxygen as the final step leading to ozone[25]. Doping SnO_2 with Sb significantly improves the reactivity of the former with respect to, for example, the chemical combustion of CO[26], with 50% of the oxygen being supplied from adsorbed molecular oxygen and 50% from the SnO_2 lattice. Further, adsorbed molecular oxygen adsorbs on oxygen vacancies associated with Sb(III) ions[27].

With respect to the process taking place at temperatures > 150 °C, assuming the same surface area of 50 m^2 g^{-1} and 9.1 x 10^{14} Sn atoms cm^{-2}, a further loss of 0.8% of the mass at 150 °C in Fig. 1(a), and 0.7% of that at the same temperature in Fig. 3(a) would be expected if all the surface Sn-OH groups underwent condensation according to equation (3). The observed losses are 1.4% and 1.3%, respectively which, given the crude nature of the calculation, does not seem unreasonable agreement.

In order to further elucidate the processes taking place during the heating of SnO_2, *in-situ* FTIR experiments were carried out.

3.3 FTIR Studies

Fig. 4 shows spectra collected during the heating of 20 mg of tin oxide diluted with 80 mg spectroscopic KBr up to 600 ºC. As can be seen from the figure, there are a number of bands superimposed upon a curving baseline. With respect to the latter, Fig. 5 shows a plot of the Kubelka-Munk function at 2000 cm^{-1}, normalised to its value at 25 ºC (the raw data are plotted in Fig. S3). This is discussed in more detail below; first, the loss of adsorbed water is considered.

Adsorbed water

From Fig. 4, it can be seen that, up to 150 ºC, there is a clear decrease in the band at 1633 cm^{-1} and the broad absorptions between 2500 cm^{-1} and 3800 cm^{-1} corresponding to the loss of some form of water[28]. The 1633 cm^{-1} H-O-H deformation is lost at T ≥ 150 ºC, suggesting the loss of adsorbed water that is complete by this temperature, in agreement with the literature[14, 29]. There is also a clear gain feature at 3479 cm^{-1}, and gain features at 3523 and 3552 cm^{-1} that become more clearly resolved as the temperature is increased and the overlying, broad O-H absorption of water is lost. In order to highlight the changes in the spectra in Fig. 4 up to 150 ºC more clearly, the spectrum collected at 25 ºC was subtracted from those taken at higher temperatures, and the results are presented in Fig. 6.

An important point to note about Fig. 6 is that, in agreement with the TGA data (see Fig. 1(b)) the spectrum collected at 50 °C (just on the differential TGA minimum) is different to those taken at 100 °C and 150 °C, suggesting that transitions in the behaviour of the SnO_2 are signalled by the minima at 63 °C and 450 °C in Fig. 1(b). As can be seen from Fig. 6, the bands at 3444 cm^{-1}, 2250 cm^{-1} and 1633 cm^{-1} are at approximately the same frequencies as those of the absorptions of liquid or bulk water[28]; however, the width and shape of the broad feature at 3444 cm^{-1} strongly suggests

that the absorptions are not due to this form, as may be expected from the low coverage. Al-Abadleh and Grassian[30] have reported infrared data on water adsorbed at Al_2O_3. These authors observed similar features to those in Fig. 6 at 3420 cm^{-1}, 2136 cm^{-1} and 1642 cm^{-1} and, by comparison with the spectra of various forms of ice, they attributed the absorptions to adsorbed ordered water. Devlin and co-workers[31] attribute the 2250 cm^{-1} band in ice to the 2nd overtone of the librational mode; they also postulate that the intensity of the O-H deformation decreases with depth into the ice and hence the 1630 cm^{-1} band in Fig. 6 may be attributed to water molecules having dangling O-H bonds at the surface[32, 33].

A comparison of the spectra collected at 50 ºC, 100 ºC and 150 ºC in Fig. 6 shows that the latter two have additional broad loss features near 3000 cm^{-1}, 2750 cm^{-1} and 1900 cm^{-1}; these have been observed by other groups and have been attributed to the O-H stretches of hydrogen-bonded Sn-OH groups[15]. From Figs. 4 and 6, it is clear that there are sharp gain features at 3658 cm^{-1} and 3552 cm^{-1}, and these may be attributed to the O-H stretches of isolated Sn-O-H groups: such features have been observed at 3610 cm^{-1} – 3640 cm^{-1} [15], 3647 cm^{-1} [34], 3620 cm^{-1}, 3595 cm^{-1} and 3560 cm^{-1} [35].

The data in Fig. 6 can be interpreted on the basis of models suggested by Morishige and co-workers[18] and Morimoto *et al.*[19, 20]. These authors interpret the spectral data with reference to the three main low index surfaces of SnO_2, namely (100), (110) and (111). The fully hydroxylated (100) surface contains OH groups in which the H atoms are sunk somewhat into the hollow sites between the oxygen atoms. Hence, the OH groups on this surface do not form hydrogen bonds to any significant extent with physisorbed water molecules, thus allowing the latter to form 2-dimensionally condensed layers on top of the "inert" OH monolayer. In contrast, the OH groups of the (110) plane point outwards perpendicularly from the surface and hence form hydrogen bonds with adsorbed water. The (111) surface is slightly more complicated, but the OH groups again point outwards and hence also form hydrogen bonds with physisorbed water. As a consequence of these interactions, water adsorbs more strongly on the (111) and (110) facets than the (100) facets. It does not seem unreasonable, therefore, to postulate that the water lost at 50 ºC showing the ice-like structure in Fig. 6 is that on the (100) facets of the nanoparticles. The water lost between 50 and 150 ºC is that which was hydrogen-bonded to the OH groups on the (111) and (110) facets. Loss of water from the (100) facets does not "release" OH groups from hydrogen bonding, hence there is no gain of absorption due to isolated OH, whereas loss of water from the (111) and (110) facets results in the gain in intensity of the bands at 3658 cm^{-1} and 3552 cm^{-1} due to appearance of isolated OH groups. The above analysis is in general agreement with the literature, where loss of physisorbed water is complete by 150 ºC[14, 15], and two forms of bound water may be identified, one more strongly bound than the other. In order to test this hypothesis, an experiment was carried out in which a reference spectrum was collected from SnO_2 in dry air, after which humidified air at 40% relative humidity was admitted, and a sample spectrum taken once equilibrium had been attained (ca. 1 hour). The result is presented in Fig. 7, and it can be seen that the spectrum strongly resembles the inverses of the spectra in Fig. 6 collected at 100 ºC and 150 ºC, supporting the postulated loss of water hydrogen-bonded to Sn-O-H groups on the surface, although there is an additional isolated OH feature at 3479 cm^{-1}. This feature is present in the spectra in Fig. 4, but its intensity does not change until temperatures above 150 °C.

The electronic absorption

Oxygen vacancies are generally accepted to be the dominant intrinsic defects in SnO_2 powders[36] and are associated with shallow donor levels lying about 0.14 eV – 0.15 eV below the conduction band minimum at low doping levels[37]. An even shallower donor at about 0.03 eV has been identified[37] and is probably associated with Sb impurities. Promotion of electrons from either of these levels into the conduction band would result in a free electron absorption with zero energy onset[38] following a $1/\nu^n$ power law[39, 40]. In SnO_2, n is generally accepted as lying between 2 and

3[40]. Clear examples of this type of absorption are given in the work of Panayotov *et al.*[39] on TiO_2 nanoparticles and the diverging shape of the spectra in Fig. 4 is very similar to the spectra in Panayotov's work, suggesting that the spectra in Fig. 4 show free electron absorption that is unaffected by heating the sample. This observation is somewhat puzzling and suggests that the electrons responsible for the long wavelength structure arise from donors that are fully ionised so that the exhaustion region has been reached. This in turn suggests that the dominant free electron absorption is associated with very shallow ionised impurity levels: in general shallow donor levels move toward the conduction band with increasing donor concentration so that levels even closer to the conduction band edge than the value of 0.03 eV alluded to above cannot be ruled out.

In addition it is clear from Figs. 4 and 5 there are broad absorption features that decrease in intensity at temperatures greater than 150 °C and which underly the vibrational bands and free electron absorption. Up to this temperature, this structure does not appear to change, as shown in Fig. 6 by the Kubelka Munk function at 4000 cm^{-1}. In order to remove the free electron absorption, and bearing in mind the temperature regions identified from the TGA data in Fig. 1(a), the spectrum collected at 150 °C was subtracted from those taken up to 450 °C, and that taken at 450 °C subtracted from those collected up to 600 °C. The resultant difference spectra are not presented here but are given as supplementary information in Figs. S4 and S5, respectively. The spectra at 450 °C in Fig. S4 and that at 600 °C in Fig. S5 are however shown in Fig. 8. As can be seen from Fig. 8, there are two broad absorptions overlying each other: one with a tail out to the near IR, and an absorption with a maximum between 4000 cm^{-1} and 1000 cm^{-1} which decrease in intensity between 150 °C and 600 °C. In an extensive series of papers, Ghiotti and co-workers[34, 35, 41, 42]studied SnO_2 powders exposed to various atmospheres using FTIR spectroscopy and observed spectra similar to those in Fig. 4. They assigned the broad absorption features to electronic transitions from donor states into the conduction band: a band with a maximum at ca. 1600 cm^{-1} was attributed to oxygen vacancies and a band at 3600 cm^{-1} to oxygen divacancies. If this interpretation is accepted the temperature variations discussed above must correspond to thermal excitation of electrons out of donor states, with a corresponding decrease in absorption intensity.

Pursuing this analysis further it is instructive to plot the logarithm of the apparent absorbance derived from the Kubleka –Munk function against 1/T. Such a plot is shown in Fig. S6 for the absorbance at 2000 cm^{-1}. The plot is linear, with a slope corresponding to a value of 0.15 eV for the thermal excitation energy for exhaustion of donor states. This value is the same as the energy difference between the oxygen vacancies and conduction band. Superficially it is surprising that large changes in the population of doubly occupied donor states can occur over the temperature range studied as the Boltzmann factor $B = exp\text{-}(\Delta E/k_BT)$ for an excitation with ΔE = 0.15 eV changes from 0.003 to only 0.136 as the temperature T increases from 298K to 873 K (25 °C to 600 °C). However it must be remembered that the extent of exhaustion of donor states is critically dependent on the concentration of donor states N_D as compared to the number of thermally accessible conduction band states N_C. For low donor levels almost complete exhaustion may be found even when the Boltzmann factor is quite small. The thermal equilibrium between free carriers with concentration n and the number of unionised donor states $N_D - n$ may be expressed in terms of an equilibrium constant K expressed[43] as:

$$K = n^2/(N_D - n) = N_C\, exp\text{-}(\Delta E/k_BT)$$

where k_B is the Boltzmann constant and N_c is itself given by:

$$N_C = 2(2\pi k_BTm_e^*/h^2)^{3/2}$$

$_{me}$* is the electron effective mass at the bottom of the conduction band. The expression for K omits the factor of 2 in the denominator which accounts for spin degeneracy of a singly occupied donor level, since we are dealing with non-degenerate, doubly occupied oxygen vacancies. The quadratic equation for *n* may be solved as a function of *T* and N_D to obtain values for the degree of exhaustion n/N_D. Some typical results are shown in Fig. S7. In all cases the ratio increases with increasing temperature and approaches 1 at sufficiently high temperatures. For low donor levels (i. e. $N_D = 10^{14}$ cm^{-3}) exhaustion is essentially complete even at room temperature, whilst for $N_D = 10^{20}$ cm^{-3} the ratio reaches only 0.1 at 1000 K. For intermediate values around 10^{17} cm^{-3} the ratio increases significantly over the temperature range between 300 K and 900 K.

The vibrational bands

Fig. 7 clearly shows that the O-H deformations associated with the bands at 3479 cm^{-1}, 3658 cm^{-1} and 3552 cm^{-1} in Figs. 4 & 8 are too weak to be detected. In Figs. S4, S5 and 8, the 3552 cm^{-1} and 3479 cm^{-1} features appear as losses as the Sn-OH species condense to release water: in Fig. S4, gain features around 1520 cm^{-1} and 1420 cm^{-1} may be discerned that appear clearly as loss features in Fig. S5 and we tentatively attribute these to overtones of asymmetric Sn-O-Sn vibrations[44].

There is a clear loss of a broad feature with a maximum around 3000 cm^{-1} in the spectra in Figs. S4, S5 and 8, which appears to be associated with the 1250 cm^{-1} loss; the latter may be attributed to an Sn-O-H deformation[44] and the former to the associated O-H stretch of strongly bound OH groups. We tentatively attribute these bands to the Sn-OH groups on the (100) facets. The breadth of the O-H stretch suggests some hydrogen bonding between Sn-O-H groups, but not as extensive as that associated with the hydrogen bonding between the Sn-OH and H_2O on the more "open" structures on the (111) and (110) facets.

From Figs. S4 and 8, it can be seen that, between 150 °C and 450 °C, loss features at 1106 cm^{-1} and 1187 cm^{-1} increase in intensity. McAleer *et al.*[45] postulate that the desorption of $O_2^{\cdot -}$ from SnO_2 takes place around 150 ºC and its conversion to O^- around 160 ºC, whilst Gundrizer and Davydov[46] attribute peaks at 1045, 1100 and 1190 cm^{-1} to $O_2^{\cdot -}$ adsorbed at various Sn sites on particulate SnO_2 (their sample having a similar surface area to the sample employed in this work). Thus, the 1106 and 1187 cm^{-1} bands in Fig. 6 may be due to the loss of $O_2^{\cdot -}$ adsorbed at various sites and its conversion to O^-.

The broad gain feature near 930 cm^{-1} may be due to lattice vibrations[44].

In order to confirm the assignments of the various features in the IR spectra, the experiment depicted in Fig. 4 was repeated using an atmosphere created by bubbling 80%N_2 + 20%O_2 through D_2O, and the spectra so obtained are shown in Fig. 9. As can be seen, the spectra are qualitatively the same allowing for the expected shift in the H_2O and isolated Sn-OH absorptions, thus there is clearly a loss of physisorbed D_2O, the loss of two electronic bands with maxima in the mid-IR and one with a tail out to 6000 cm^{-1} that stops being lost at 450 °C and the free electron absorption that does not change with temperature. Fig. S8 shows the spectrum collected at 25 °C subtracted from those taken up to 150 °C, i. e. analogous to Fig. 6. The O-H stretch and deformation of the physisorbed water are shifted to lower frequencies by a factor of 1.35 when using D_2O, as would be expected. The 1260 cm^{-1} feature is absent from both Figs. S8 and 9, suggesting the vibration responsible involves hydrogen.

Fig. S9 shows the spectrum collected at 150 °C in Fig. 9 subtracted from those taken at temperatures between 200 and 450 °C and Fig. 10 shows the spectrum collected at 450 °C in Fig. S9 and that collected at the same temperature in Fig. S4, the latter scaled (increased) by a factor of 1.27 for comparison. The peak attributed to the SnO-H loss feature due to species on the (100)

facets has shifted by a factor of 1.35 to lower frequency, suggesting the assignment is valid; again, the 1250 cm^{-1} band is absent, presumably shifted below the cut-off of the spectrometer. The frequencies of the isolated SnO-H loss features at 3552 and 3479 cm^{-1} are also shifted to lower values by a factor of 1.35. The sharp bands around 3500 cm^{-1} on both spectra are most likely due to the plastic coating on the beamsplitter of the FTIR.

The 1179 cm^{-1} loss feature is present in both spectra in Fig. 10, supporting its assignment to Sn-O-O, whilst the 1106 cm^{-1} band is absent from the D_2O spectrum, and hence may be due to Sn-O-O-H. The 930 cm^{-1} band does not move and hence may be due to lattice vibrations, as postulated.

4. CONCLUSIONS

SnO_2 prepared by a hydrothermal method and calcined at 400 ºC shows only the cassiterite structure with a BET surface area of 50 $m^2\ g^{-1}$. At room temperature, water adsorbs in essentially two forms according to the facets of the underlying SnO_2. Thus, water on the (100) facets cannot hydrogen bond with the Sn-OH moieties as the hydrogen atoms of the latter are concealed below the surface, and hence form two-dimensional ice-like structures. Water is more strongly adsorbed on the (111) and (110) facets due to hydrogen bonding. Two types of electronic absorption are observed: free electron absorptions associated with exhausted very shallow ionised impurity levels and absorptions from oxygen vacancies below the conduction band. Surprisingly, the former appear not to be temperature-dependent. The behaviour of the absorptions arising from the oxygen vacancies may be interpreted in terms of a model involving the thermal equilibrium between free carriers and un-ionised donor states, wherein exhaustion of the donor states is complete at low carrier concentrations and room temperature, whilst the ratio reaches only 0.1 at high concentrations and 1000K. Finally, and importantly, oxygen adsorbs onto SnO_2, even when adsorbed water is present, and this is of direct relevance to the mechanism of ozone formation at NATO anodes.

AUTHOR INFORMATION

Corresponding Author
*E-mail paul.christensen@ncl.ac.uk

Notes
The authors declare no competing financial interest.

SUPPORTING INFORMATION

The Supporting Information contains XRD data and additional FTIR data.

ACKNOWLEDGEMENTS

SM would like to thank the Thai Government for the award of a Royal Thai Scholarship. The authors would like to thank Mr. Bernard Bowler for his expertise in thermogravimetric analysis.

REFERENCES

1. R. Y. Khoudja, Y. Xu, T. Li and C. Zhou, *Journal of Assisted Reproduction and Genetics*, 2013, **30**, 69-76.
2. P. A. Christensen, T. Yonar and K. Zakaria, *Ozone-Science & Engineering*, 2013, **35**, 149-167.
3. S.A. Cheng and K.Y. Chan, *Electrochemical and solid-state letters*, 2004, **7**, D4-D6.
4. Y. H. Wang, S. A. Cheng, K. Y. Chan and X. Y. Li, *Journal of the Electrochemical Society*, 2005, **152**, D197-D200.
5. P. A. Christensen, W. F. Lin, H. Christensen, A. Imkum, J. M. Jin, G. Li and C. M. Dyson, *Ozone: Science & Engineering*, 2009, **31**, 287-293.
6. M. Pourbaix, *Atlas of electrochemical equilibria in aqueous solutions*, National Association of Corrosion Engineers, Houston, Tex., 1974.
7. Y. H. Wang, K. Y. Chan, X. Y. Li and S. K. So, *Chemosphere*, 2006, **65**, 1087-1093.
8. J. Basiriparsa and M. Abbasi, *Journal of Solid State Electrochemistry*, 2012, **16**, 1011-1018.
9. S. Y. Yang, Y. S. Choo, S. Kim, S. K. Lim, J. Lee and H. Park, *Applied Catalysis B-Environmental*, 2012, **111**, 317-325.
10. S. Fujihara, T. Maeda, H. Ohgi, E. Hosono, H. Imai and S.-H. Kim, *Langmuir*, 2004, **20**, 6476-6481.
11. P. A. Christensen and S. W. M. Jones, *Polymer Degradation and Stability*, 2014, **105**, 211-217.
12. P. Kubelka, *J. Opt. Soc. Am.*, 1948, **38**, 448-457.
13. C. Pijolat, P. Breuil, A. Méthivier and R. Lalauze, *Sensors and Actuators B: Chemical*, 1993, **14**, 646-648.
14. P. G. Harrison and A. Guest, *Journal of the Chemical Society, Faraday Transactions 1: Physical Chemistry in Condensed Phases*, 1987, **83**, 3383-3397.
15. E. W. Thornton and P. G. Harrison, *Journal of the Chemical Society, Faraday Transactions 1: Physical Chemistry in Condensed Phases*, 1975, **71**, 461-472.
16. I. Saadeddin, H. S. Hilal, B. Pecquenard, J. Marcus, A. Mansouri, C. Labrugere, M. A. Subramanian and G. Campet, *Solid State Sciences*, 2006, **8**, 7-13.
17. P. H. Emmett and H. E. Ries, *Catalysis 1: Fundamental Principles*, Reinhold Publishing Corporation, 1954.
18. K. Morishige, S. Kittaka and T. Morimoto, *Bulletin of the Chemical Society of Japan*, 1980, **53**, 2128-2132.
19. T. Morimoto, Y. Yokota and S. Kittaka, *The Journal of Physical Chemistry*, 1978, **82**, 1996-1999.

20. T. Morimoto, M. Kiriki, S. Kittaka, T. Kadota and M. Nagao, *The Journal of Physical Chemistry*, 1979, **83**, 2768-2770.
21. S. Higgins, N. M. Sammes, A. Smirnova, J. A. Kilner and G. Tompsett, *Journal of Fuel Cell Science and Technology*, 2008, **5**, 011003-011003.
22. H.W. Wang, D. J. Wesolowski, T. E. Proffen, L. Vlcek, W. Wang, L. F. Allard, A. I. Kolesnikov, M. Feygenson, L. M. Anovitz and R. L. Paul, *Journal of the American Chemical Society*, 2013, **135**, 6885-6895.
23. C. M. Aldao, F. Schipani, M. A. Ponce, E. Joanni and F. J. Williams, *Sensors and Actuators B: Chemical*, 2014, **193**, 428-433.
24. J. Mizusaki, H. Koinuma, J.-I. Shimoyama, M. Kawasaki and K. Fueki, *Journal of Solid State Chemistry*, 1990, **88**, 443-450.
25. L. M. Da Silva, L. A. De Faria and J. F. C. Boodts, *Electrochimica Acta*, 2003, **48**, 699-709.
26. B. Slater, C. R. A. Catlow, D. H. Gay, D. E. Williams and V. Dusastre, *The Journal of Physical Chemistry B*, 1999, **103**, 10644-10650.
27. K. Sun, J. Liu and N. D. Browning, *Journal of Catalysis*, 2002, **205**, 266-277.
28. K. Rahmelow and W. Hubner, *Applied Spectroscopy*, 1997, **51**, 160-170.
29. P. G. Harrison and M. J. Willett, *Journal of the Chemical Society, Faraday Transactions 1: Physical Chemistry in Condensed Phases*, 1989, **85**, 1921-1932.
30. H. A. Al-Abadleh and V. H. Grassian, *Langmuir*, 2003, **19**, 341-347.
31. J. P. Devlin, J. Sadlej and V. Buch, *The Journal of Physical Chemistry A*, 2001, **105**, 974-983.
32. J. P. Devlin and V. Buch, *The Journal of Physical Chemistry B*, 1997, **101**, 6095-6098.
33. J. Hernandez, N. Uras and J. P. Devlin, *The Journal of Chemical Physics*, 1998, **108**, 4525-4529.
34. G. Ghiotti, A. Chiorino and F. Boccuzzi, *Sensors and Actuators*, 1989, **19**, 151-157.
35. G. Ghiotti, A. Chiorino and W. Xiong Pan, *Sensors and Actuators B: Chemical*, 1993, **16**, 367-371.
36. J. Maier and W. Göpel, *Journal of Solid State Chemistry*, 1988, **72**, 293-302.
37. S. Samson and C. G. Fonstad, *Journal of Applied Physics*, 1973, **44**, 4618-4621.
38. T. Nütz, U. z. Felde and M. Haase, *The Journal of Chemical Physics*, 1999, **110**, 12142-12150.
39. D. A. Panayotov, S. P. Burrows and J. R. Morris, *The Journal of Physical Chemistry C*, 2012, **116**, 4535-4544.
40. R. Summitt and N. F. Borrelli, *Journal of Physics and Chemistry of Solids*, 1965, **26**, 921-925.
41. C. Ghiotti, Anna, F. Boccuzzi and G. , *Sensors and Actuators B: Chemical*, 1991, **5**, 189-192.
42. G. Ghiotti, A. Chiorino, G. Martinelli and M. C. Carotta, *Sensors and Actuators B: Chemical*, 1995, **25**, 520-524.
43. S. R. Elliott, *The physics and chemistry of solids*, John Wiley and Sons Ltd, Chichester, United Kingdom, 2000.
44. D. Amalric-Popescu and F. Bozon-Verduraz, *Catalysis Today*, 2001, **70**, 139-154.
45. J. F. McAleer, P. T. Moseley, J. O. W. Norris and D. E. Williams, *Journal of the Chemical Society, Faraday Transactions 1: Physical Chemistry in Condensed Phases*, 1987, **83**, 1323-1346.
46. T. A. Gundrizer and A. A. Davydov, *Reaction Kinetics and Catalysis Letters*, 1975, **3**, 63-70.

FIGURE CAPTIONS

1. (a) The thermogravimetric response of 45.7 mg of SnO_2, heated in 40 cm^3 min^{-1} flowing air 5°C min^{-1} from room temperature to 900 °C. The sample was held at 900 °C for 10 minutes and then cooled at 5°C min^{-1} to room temperature. (b) Differential of the curve in (a).
2. The variation of the m/z = 18 peak during the heating of the sample in fig. 1.
3. (a) The thermogravimetric response of 56.0 mg of SnO_2, heated in 40 cm^3 min^{-1} flowing air °C min^{-1} from room temperature to 900 °C. The sample was held at 900 °C for 10 minutes and then cooled at 5°C min^{-1} to room temperature. The process was repeated a further three times (run 3 omitted for clarity). (b) Run 4 (the 4^{th} heating/cooling cycle) in Fig. 3(a).
4. FTIR spectra (8 cm^{-1} resolution, 100 co-added and averaged scans, 2 minutes per scanset) as a function of temperature during the heating of 20 mg SnO_2+80 mg KBr powder. The reference spectrum was collected from pure KBr powder at 25ºC. Other spectra collected at the temperatures shown.
5. Plot of the Kubelka-Munk function at 2000 cm^{-1} from the spectra in fig. 4.
6. The spectra in fig. 4 collected up to 150ºC. (i) 50 °C, (ii) 100 °C and (iii) 150 °C.
7. A spectrum (8 cm^{-1} resolution, 100 co-added and averaged scans, 2 minutes per scanset) collected 1 hour after admitting air at 40% Relative Humidity into the environmental chamber. The sample was 20 mg SnO_2+80 mg KBr and the reference spectrum was collected under dry N_2.
8. (i) The spectrum collected at 150 °C in fig. 4 subtracted from that taken at 450 °C, and (ii) the spectrum collected at 450 °C subtracted from that at 600 °C.
9. FTIR spectra (8 cm^{-1} resolution, 100 co-added and averaged scans, 2 minutes per scanset) as a function of temperature during the heating of 20 mg SnO_2+80 mg KBr powder. The reference spectrum was collected from pure KBr powder at 25ºC in dry N_2. Other spectra collected at the temperatures shown. The atmosphere was 80%N_2+20%O_2 passed through D_2O.
10. (i) The spectrum collected at 150 °C in fig. 9 subtracted from that taken at 450 °C. (ii) The corresponding spectrum (i) in fig. 8. The latter has been enhanced by a factor of 1.27 for clarity.

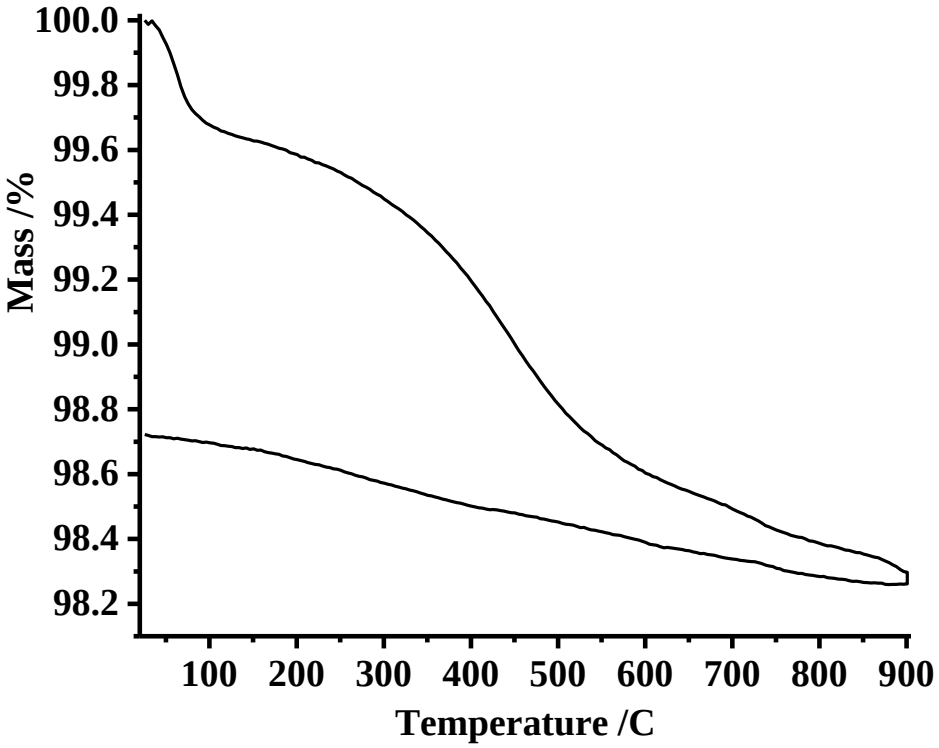
100.0
99.8
99.6
99.4
99.2
99.0
98.8
98.6
98.4
98.2
Mass /%
100
200
300
400
500
600
700
800
900
Temperature /C

(a)

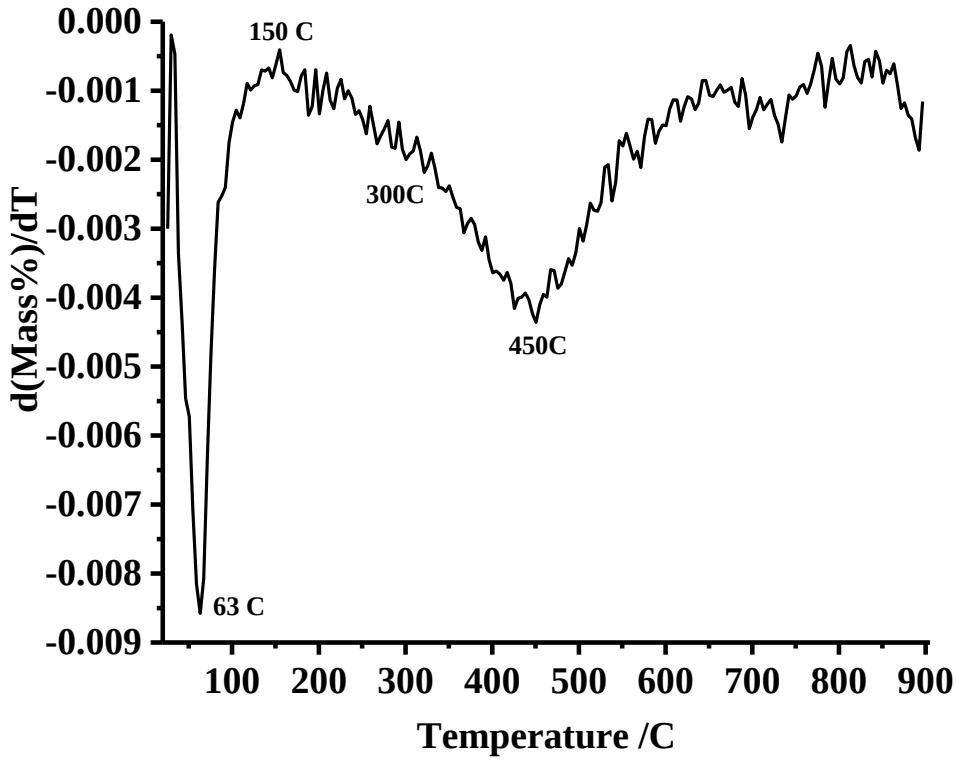
0.000
-0.001
-0.002
-0.003
-0.004
-0.005
-0.006
-0.007
-0.008
-0.009
d(Mass%)/dT
150 C
300C
450C
63 C
100
200
300
400
500
600
700
800
900
Temperature /C

(b)

Figure 1

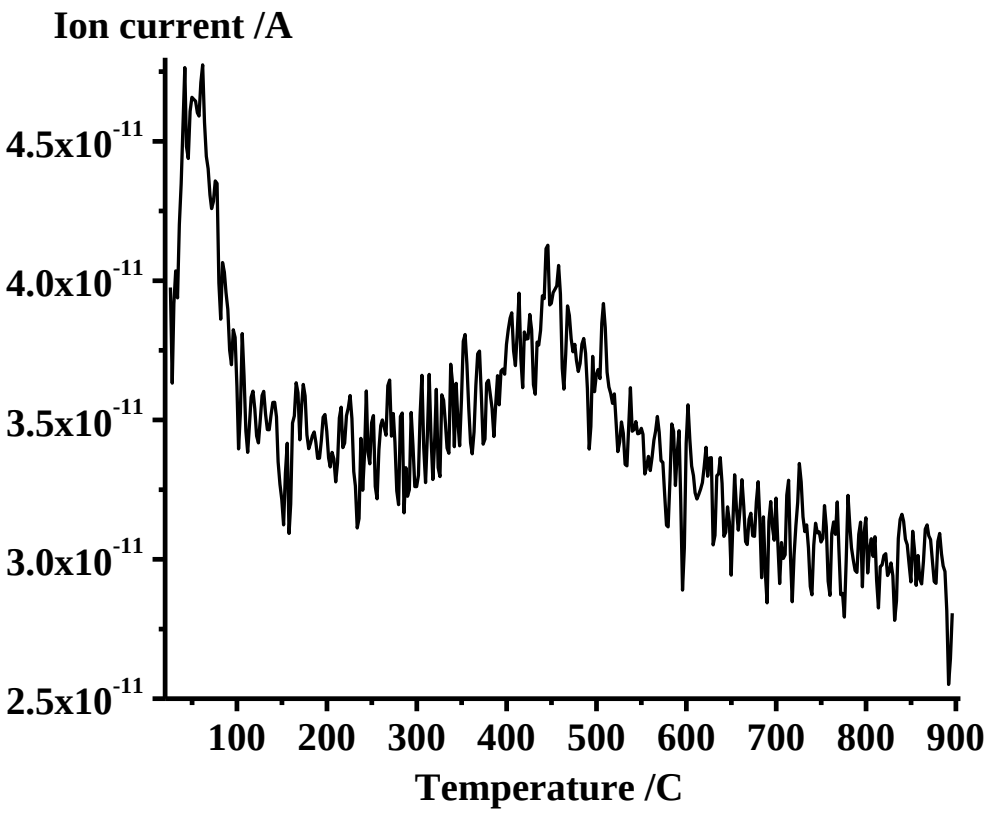
Ion current /A
4.5x10-11
4.0x10-11
3.5x10-11
3.0x10-11
2.5x10-11
100
200
300
400
500
600
700
800
900
Temperature /C

Figure 2

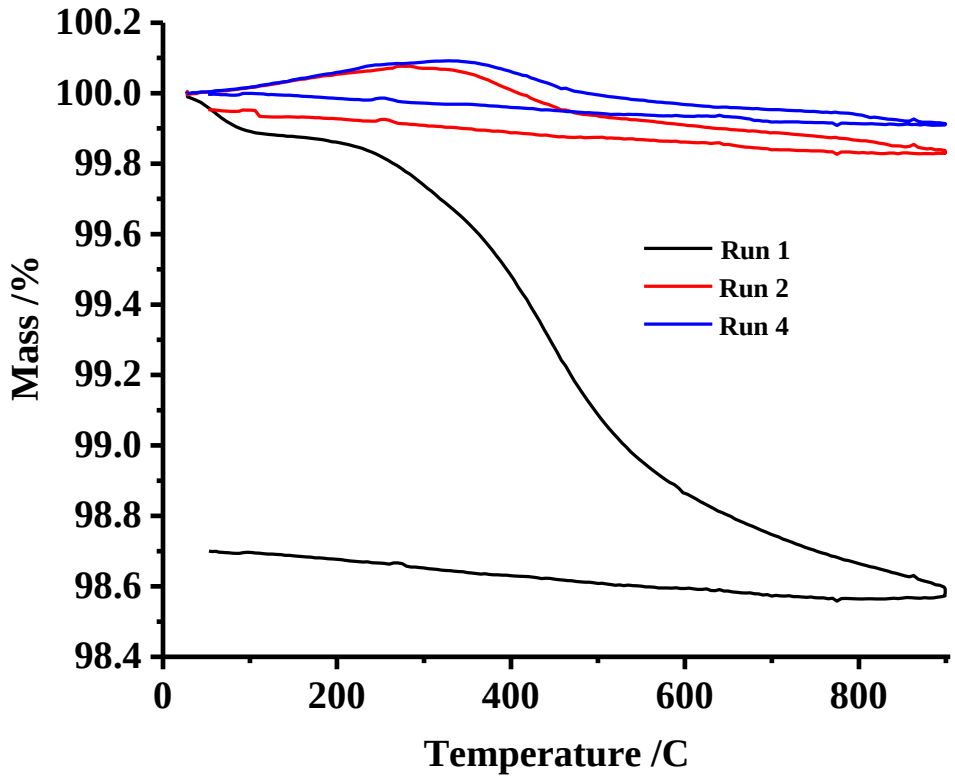
100.2
100.0
99.8
99.6
99.4
99.2
99.0
98.8
98.6
98.4
Mass /%
0
200
400
600
800
Temperature /C
Run 1
Run 2
Run 4

(a)

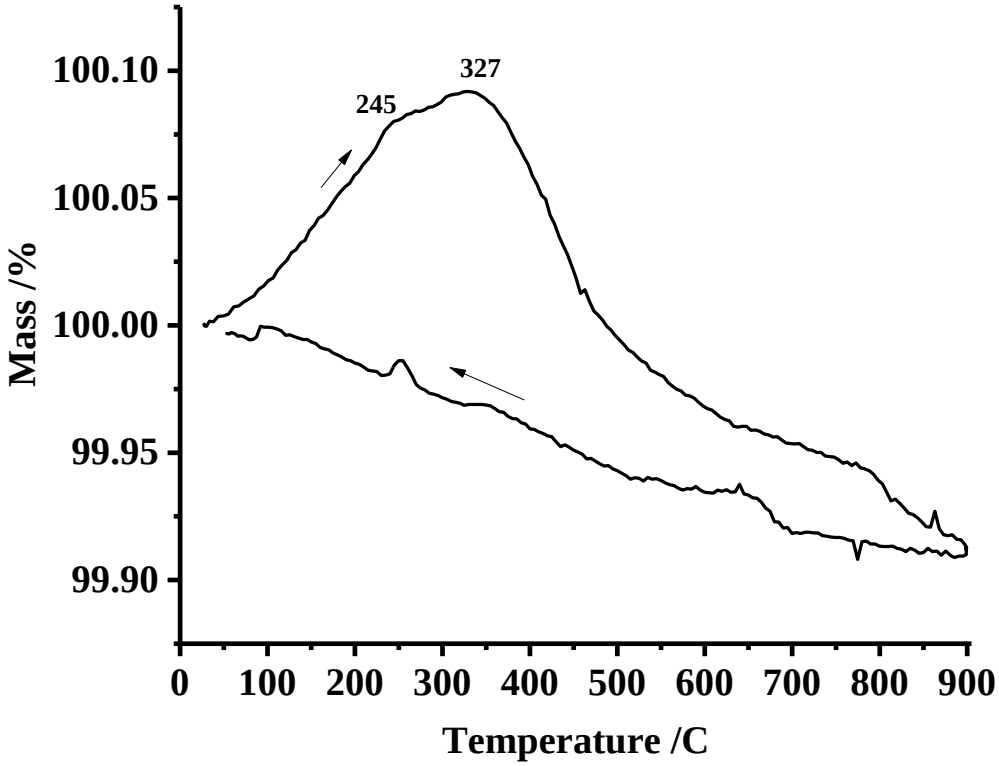

(b)

Figure 3

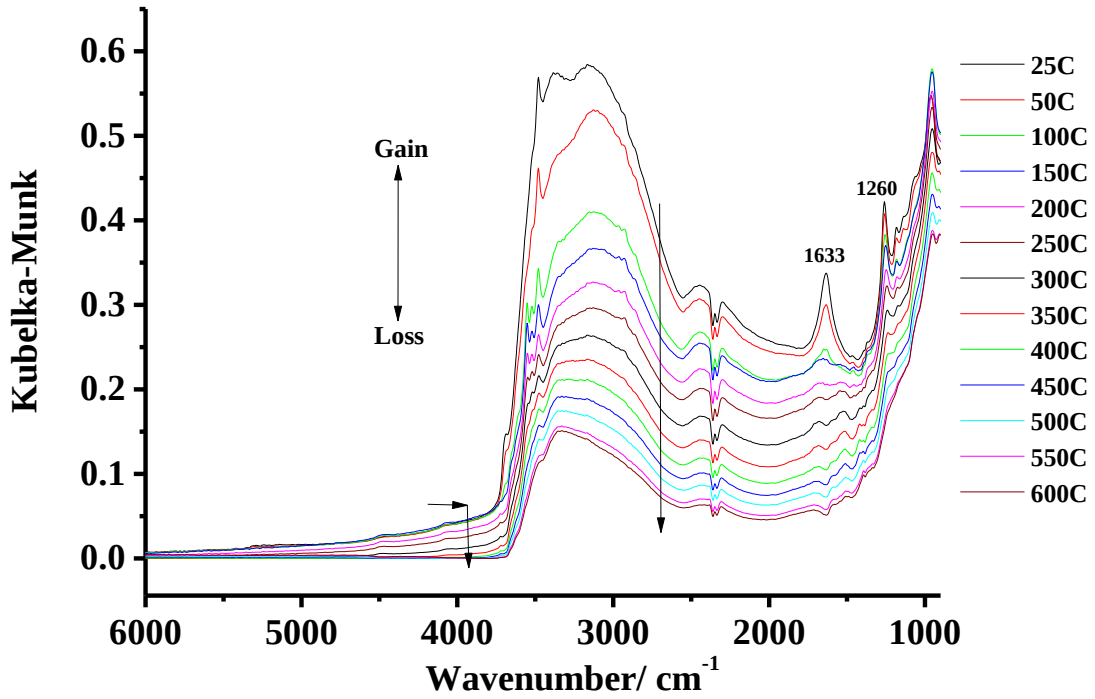

Figure 4

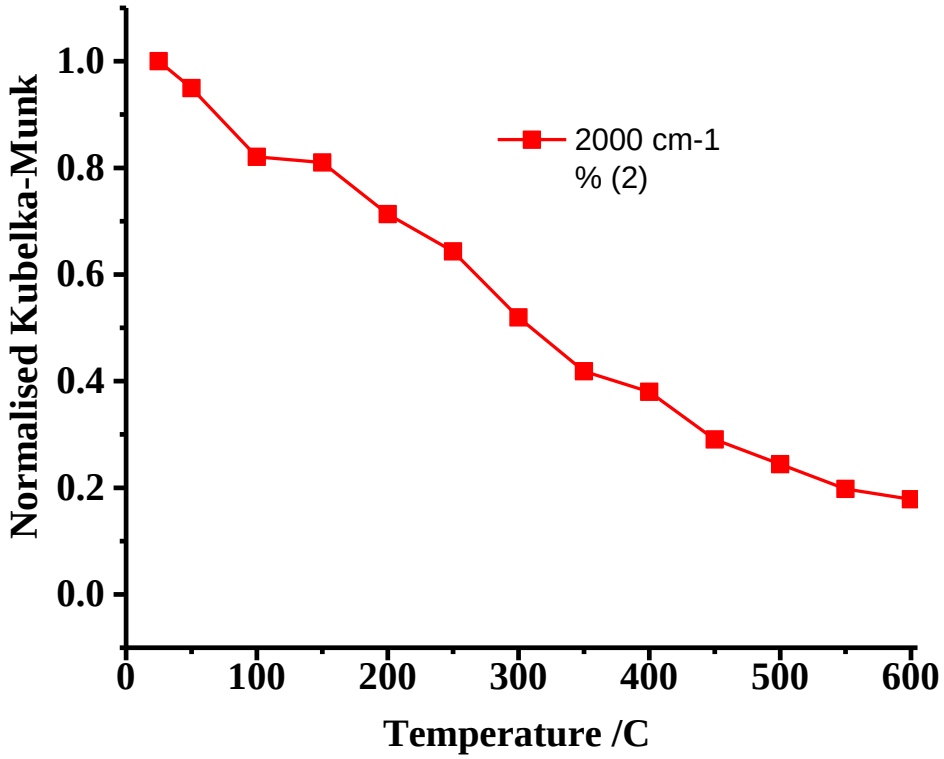

Figure 5

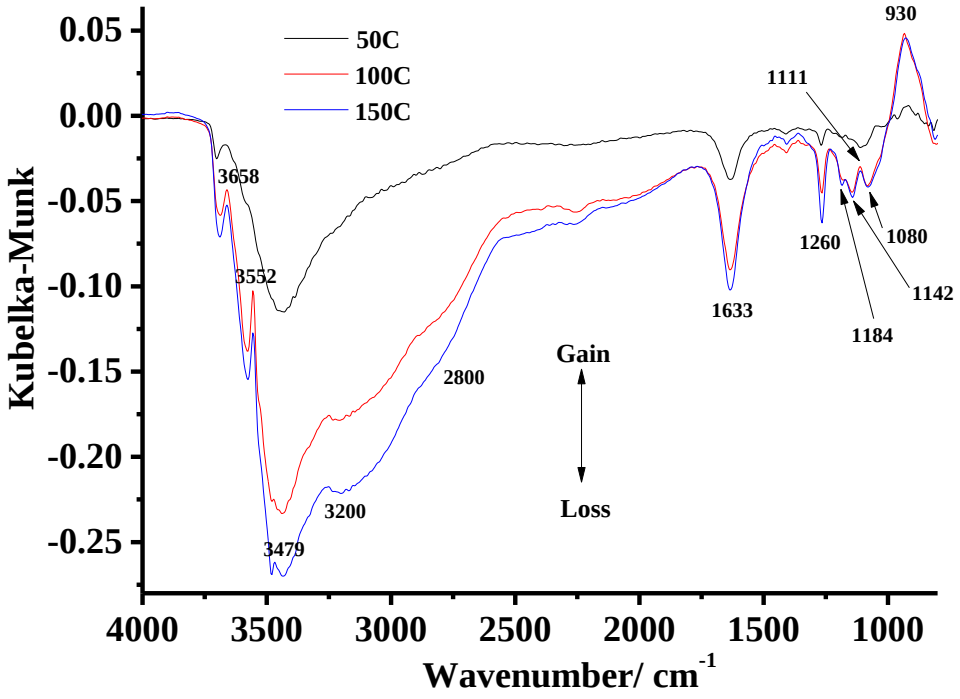

Figure 6

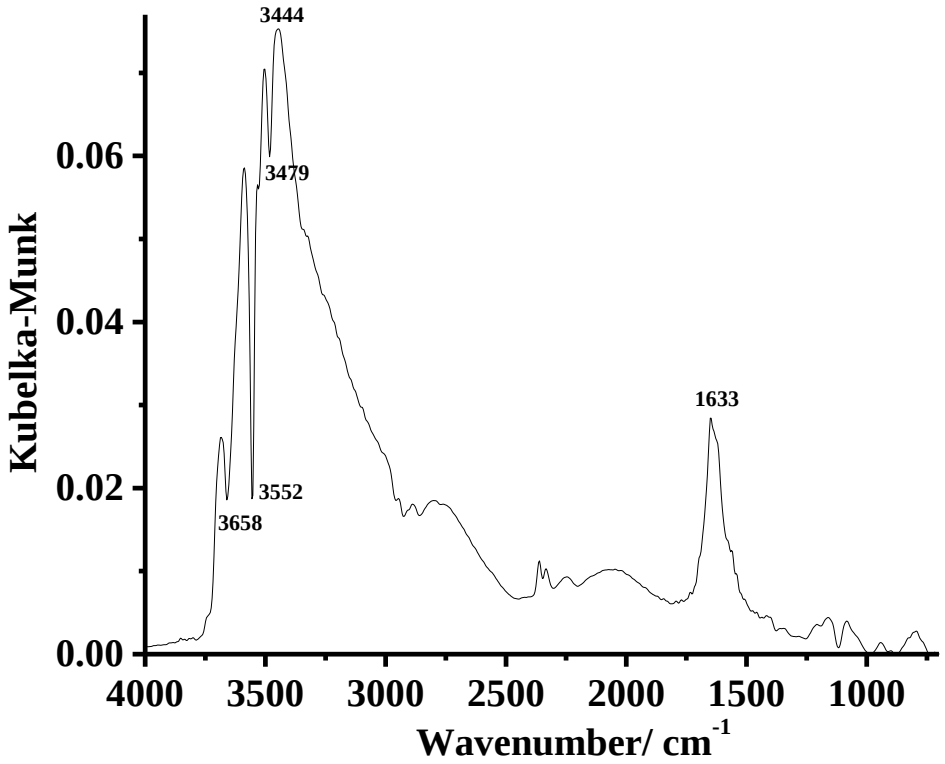

Figure 7

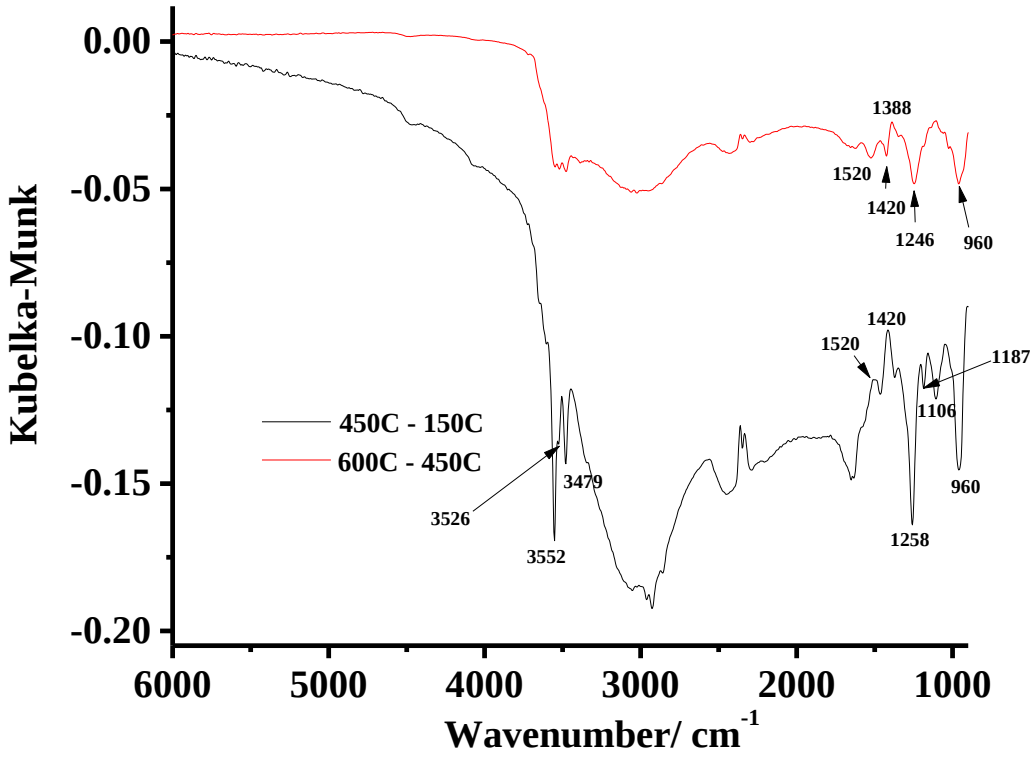

Figure 8

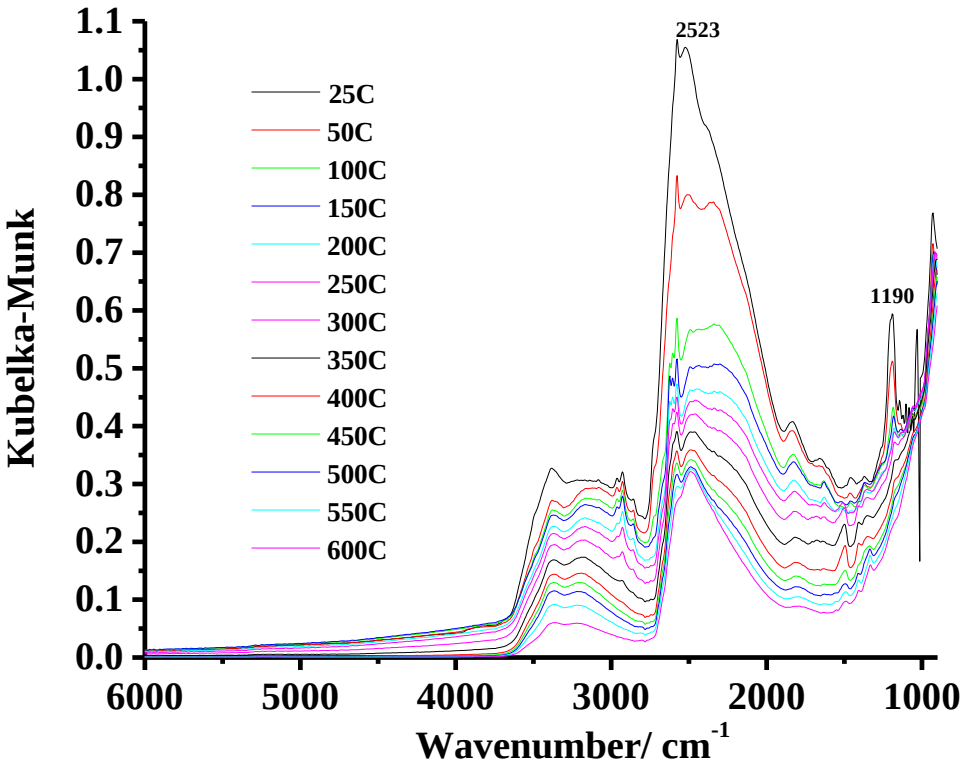

Figure 9

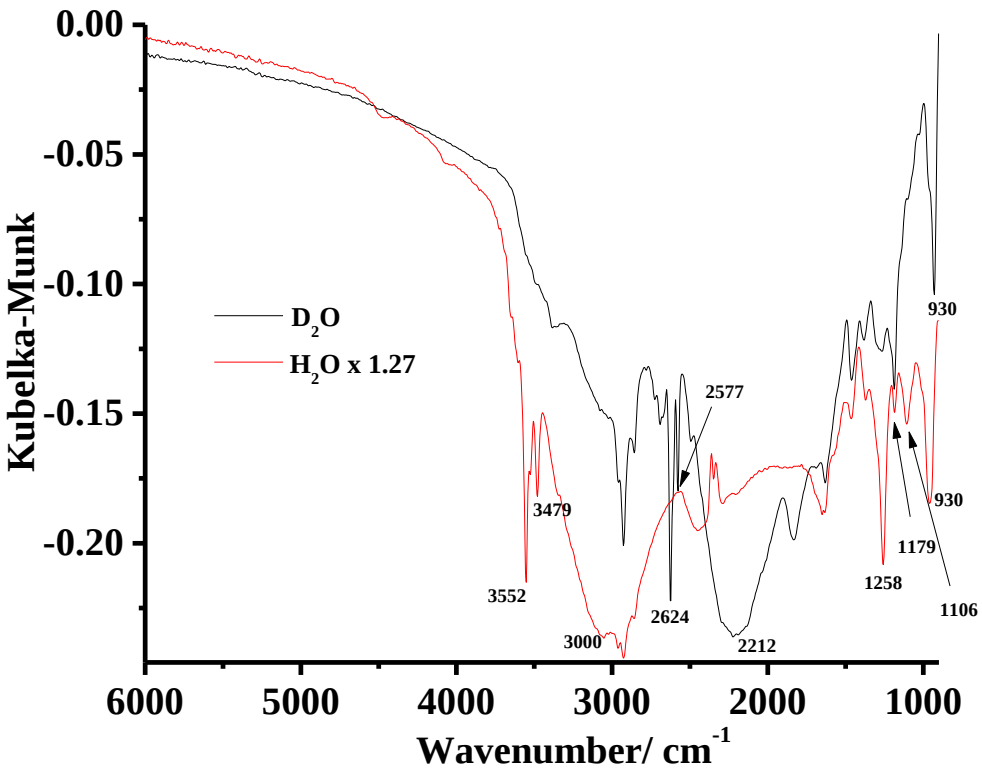

Figure 10

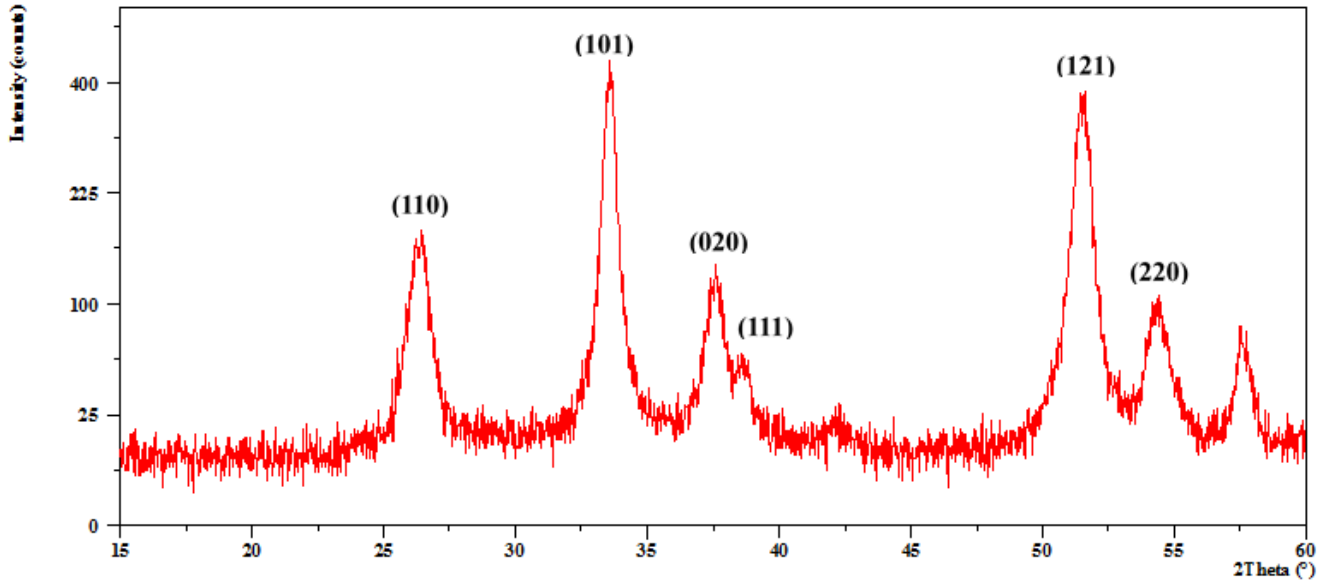

Figure S1. X-Ray Diffraction pattern of the SnO_2 nanopowder employed in this work.

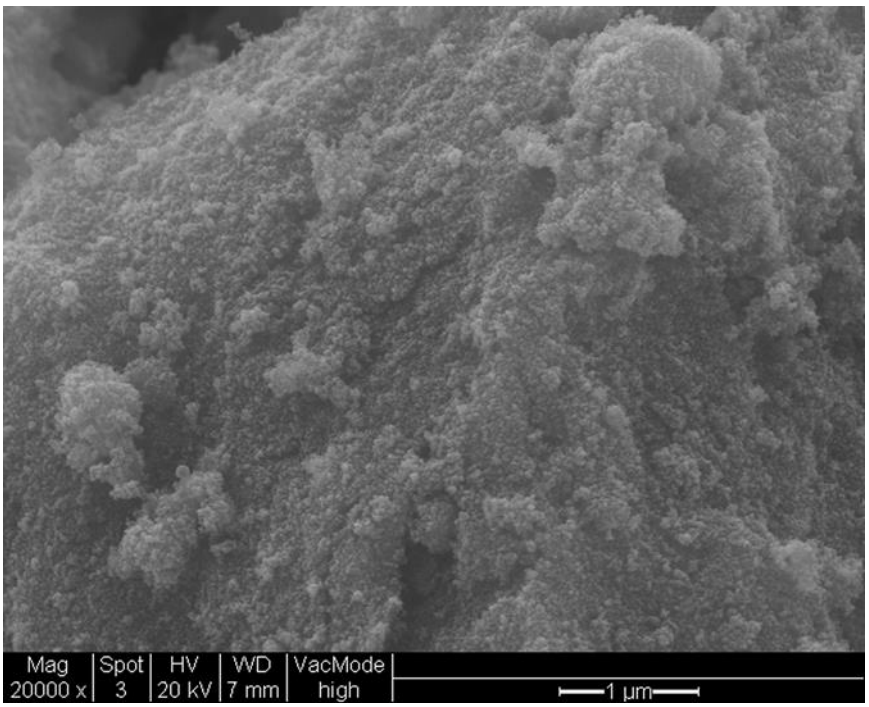

Figure S2. SEM micrograph of the SnO_2 nanopowders employed in this work, magnification x 20000.

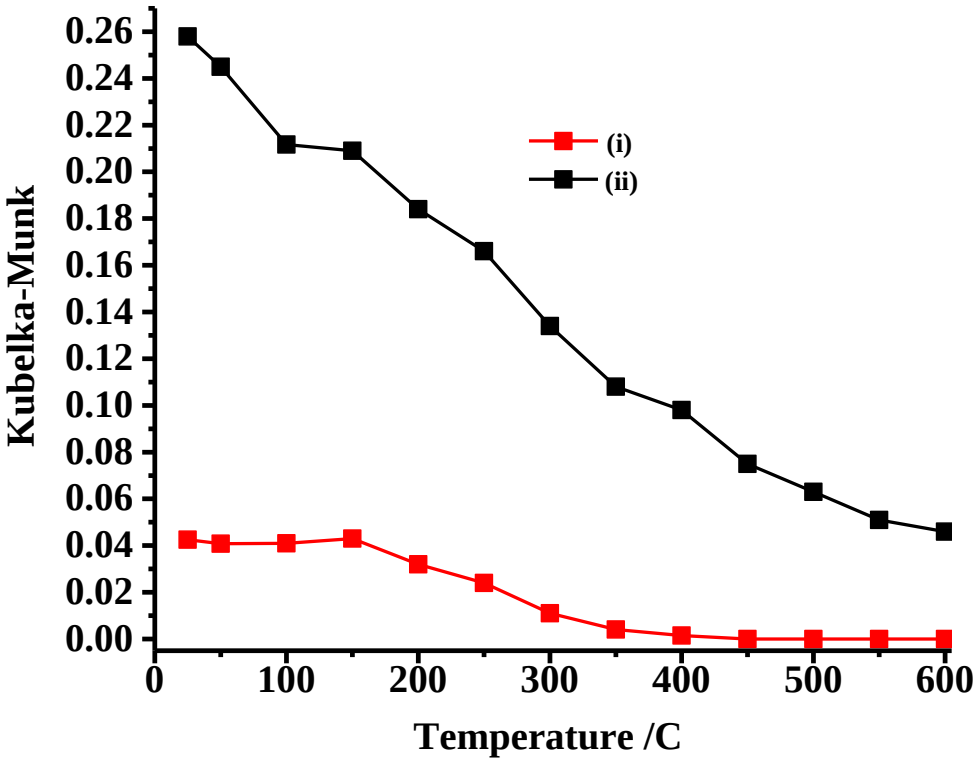

Figure S3. Plots of the Kubelka-Munk function at (i) 4000 cm^{-1} and (ii) 2000 cm^{-1} from the spectra in fig. 4.

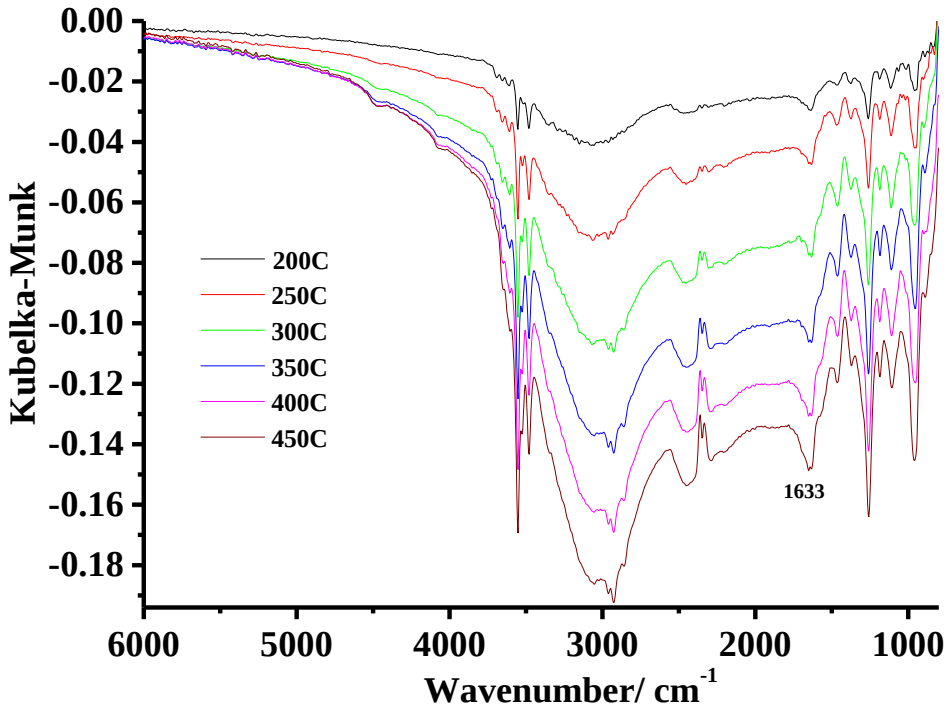

Figure S4. The spectrum collected at 150 °C in fig. 4 subtracted from those taken up to 450 °C.

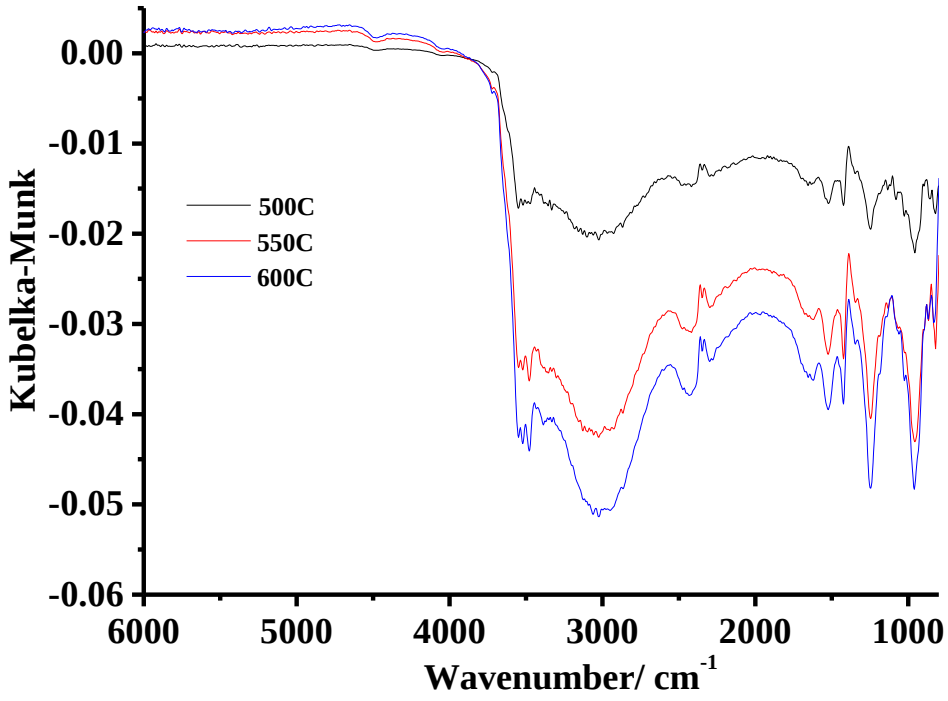

Figure S5. The spectrum collected at 450 °C in fig. 4 subtracted from those taken up to 600 °C.

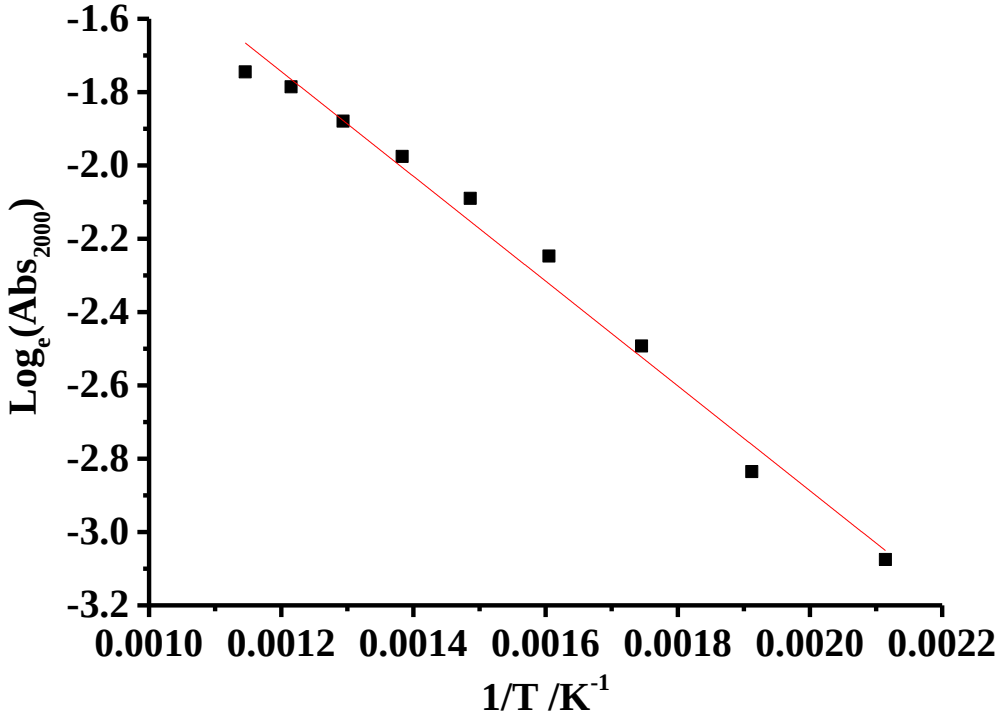

Figure S6. Plot of the natural log of the absorbance at 2000 cm^{-1} in fig. 4 vs 1/temperature.

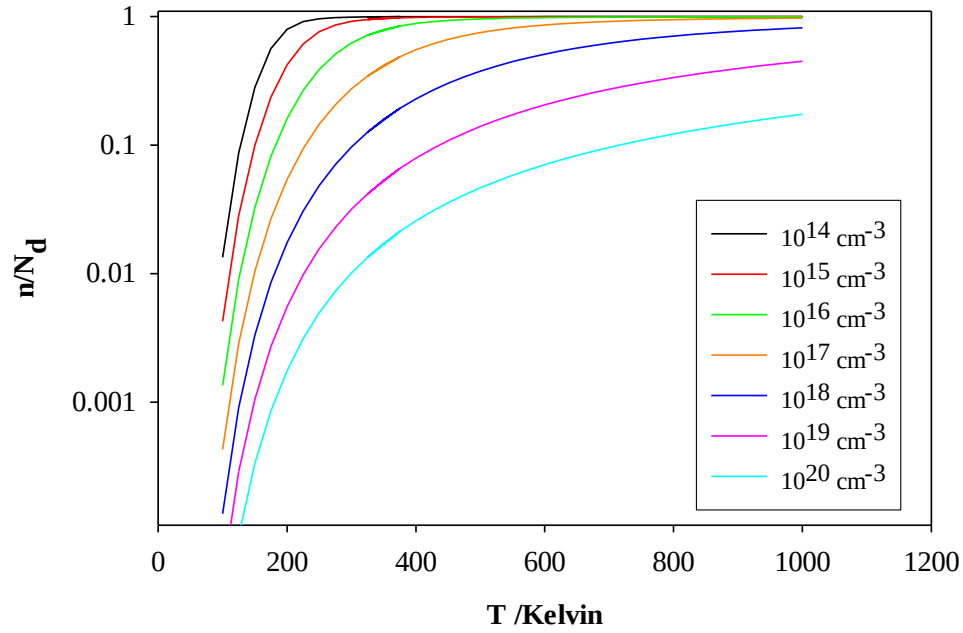

Figure S7. Plot of the fraction of ionised donor states n/N_d vs temperature, see text for details.

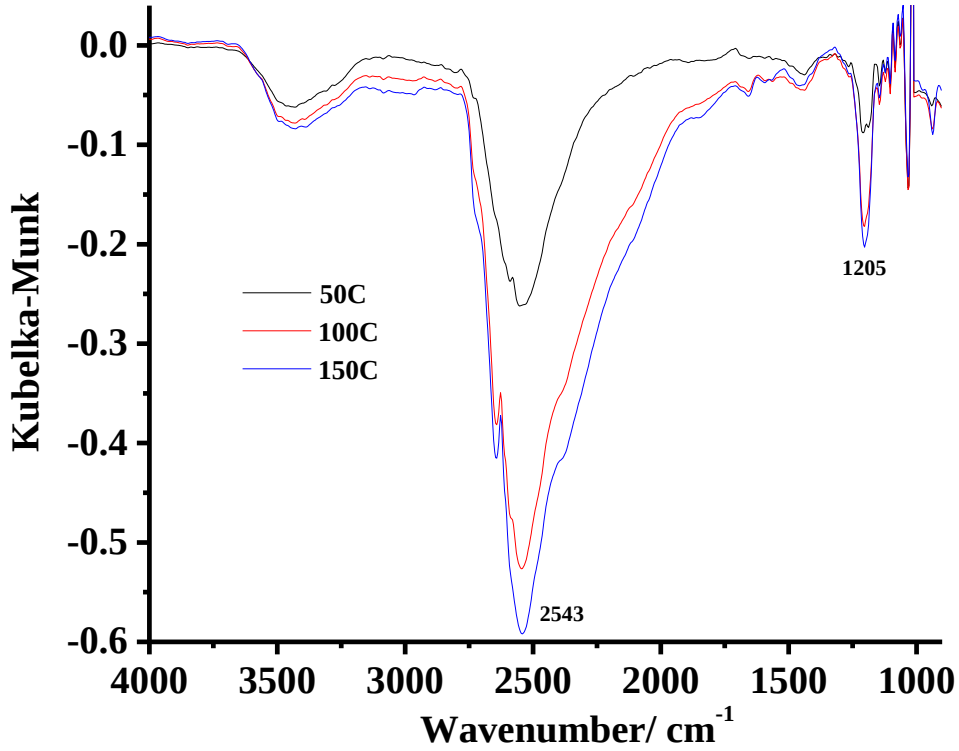

Figure S8 FTIR spectra (8 cm^{-1} resolution, 100 co-added and averaged scans, 2 minutes per scanset) as a function of temperature during the heating of 20 mg SnO_2+80 mg KBr powder. The reference spectrum was collected from pure KBr powder at 25ºC in dry N_2. Other spectra collected at the temperatures shown. The atmosphere was 80%N_2+20%O_2 passed through D_2O.

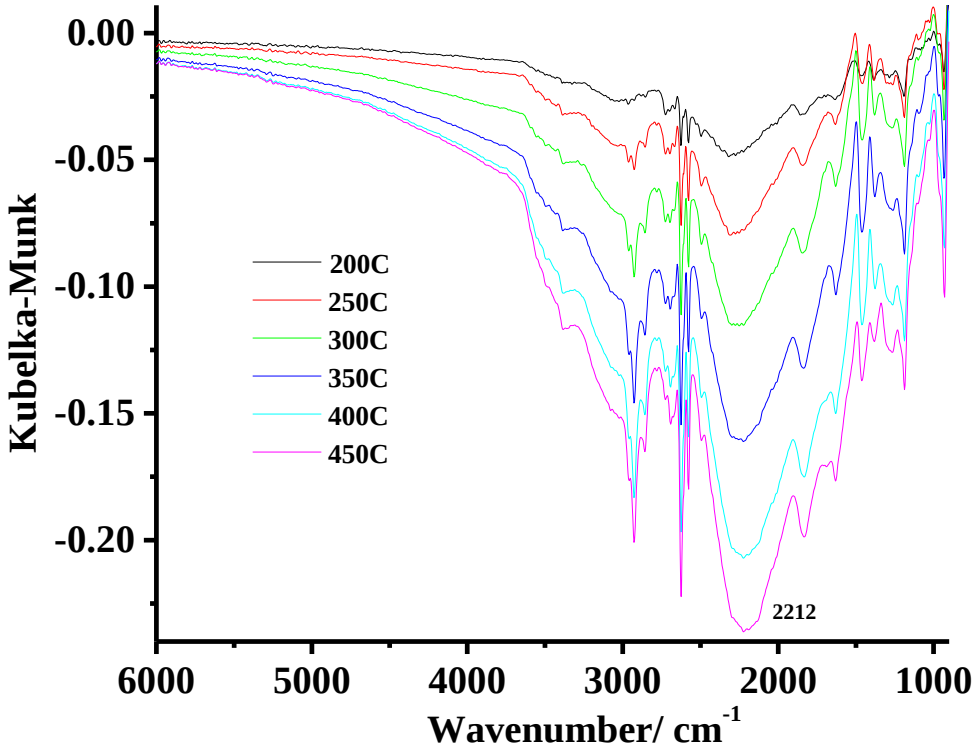

Figure S9 FTIR spectra (8 cm^{-1} resolution, 100 co-added and averaged scans, 2 minutes per scanset) collected during the experiment depicted in fig. S7. The spectrum collected at 150 °C was subtracted from the spectra taken from 200 °C to 450 °C.